Heterostructured AgX/g-C$_3$N$_4$ (X = Cl and Br) nanocomposites via a sonication-assisted deposition-precipitation approach: Emerging role of halide ions in the synergistic photocatalytic reduction of carbon dioxide

Wee-Jun Ong, Lutfi Kurnianditia Putri, Lling-Lling Tan, Siang-Piao Chai*, Siek-Ting Yong

Multidisciplinary Platform of Advanced Engineering, Chemical Engineering Discipline, School of Engineering, Monash University, Jalan Lagoon Selatan, Bandar Sunway, 47500 Selangor, Malaysia

A B S T R A C T

In this work, visible-light-active silver halide AgX(X = Cl and Br) deposited on the protonated graphitic carbon nitride (pCN) photocatalyst was developed by a sonication-assisted deposition-precipitation route at room temperature. The surface morphology, phase structure, chemical composition, optical property and electronic band structures of the AgX-hybridized pCN (AgX/pCN) hybrid nanocomposites were systematically characterized. Subsequently, the photocatalytic performance of the AgX/pCN was evaluated by the reduction of CO$_2$ to CH$_4$ in the presence of H$_2$O vapor under a low-power energy-saving daylight bulb at atmospheric pressure and ambient temperature. The optimal 30AgBr/pCN presented the highest photocatalytic activity, achieving a total CH$_4$ evolution of 10.92 μmol g$_{catalyst}$$^{-1}$, which was 34.1 and 4.2 times greater than those of single-phase AgBr and pCN, respectively. Furthermore, by comparing different halide ions, the photoactivity of 30AgBr/pCN was higher (by a factor of 1.3) than that of the optimal 30AgCl/pCN. The enhanced photocatalytic activity was accredited to (1) the surface plasmon resonance (SPR) effect from Ag and (2) the formation of heterojunction structure between pCN and AgBr in the AgBr/pCN hybrid photocatalysts for efficient charge transfer and separation to retard the recombination process as evidenced by the photoluminescence analysis. The effective charge separation was attributed to the matching of electronic band potentials of pCN and AgBr, exhibiting the Type II heterojunction, in comparison to that of AgCl/pCN (Type I heterojunction). Lastly, the plasmon-enhanced photocatalytic mechanisms associated with both Ag/AgBr/pCN and Ag/AgCl/pCN hybrid nanoarchitectures were critically discussed.

1. Introduction

Over the past few years, global warming has become a global environmental threat, which is majorly caused by the increasing anthropogenic release of carbon dioxide (CO$_2$) into the atmosphere. As a result, extensive studies aiming at reducing the concentration of CO$_2$ and converting it into energy-rich fuels have been widely researched not only for resolving environmental issues, but also for artificial photosynthesis [1,2]. The conventional conversion of CO$_2$ performed at high temperature and pressure is highly undesirable due to the fact that the activation of CO$_2$ forming hydrocarbon fuels necessitates high energy consumption of 220–330 kJ mol^{-1} [3,4]. In this regard, inspired by the natural photosynthesis in plants, photo-

catalytic reduction of CO$_2$ to energy-rich fuels utilizing clean solar energy is a promising solution to mitigate the ever-growing atmospheric concentration of CO$_2$ and meet the long-term worldwide energy demands without employing further CO$_2$-producing power sources [5].

Since the solar energy from the sunlight comprises of 43% visible light, the development of visible-light-responsive semiconductor photocatalysts has gained significant interdisciplinary attention [6]. Over the years, engineering photocatalysts for efficient CO$_2$ conversion predominantly focused on the design of metal oxide semiconductors with large band gap energies incorporating ions with empty or filled d-orbitals such as Ti^{4+}, In^{3+}, W^{6+} and Ge^{4+} [7,8]. However, most of the semiconductor materials are not active in the visible light range [9]. Hence, alternative visible-light-active photocatalysts are being enthusiastically pursued. Very recently, a metal-free visible-light-excited photocatalyst, known as graphitic carbon nitride (g-C$_3$N$_4$), has received incessant interest due to its

earth-abundant nature and high chemical stability since its first discovery by Wang et al. [10] for hydrogen production from water splitting under visible light.

Despite the aforementioned benefits of g-C_3N_4 material and photocatalytic process, the photocatalytic efficiency is still low to make the system viable for practical applications owing to the high recombination rate of photogenerated charge carriers in the individual semiconductor. Among various modifications to enhance the photoactivity, the construction of semiconductor heterojunctions by coupling g-C_3N_4 with another semiconductor with appropriate valence band (VB) and conduction band (CB) has been regarded as one of the effective strategies to reduce the recombination rate of electron–hole pairs. Considering the advantages of nanocomposite heterojunctions, numerous g-C_3N_4-based heterojunction photocatalysts have been synthesized such as ZnO/g-C_3N_4 [11], TiO_2/g-C_3N_4 [12], Bi_2WO_6/g-C_3N_4 [13] and WO_3/g-C_3N_4 [14], and demonstrated a remarkable improvement in the photocatalytic performance on the dye degradation and water splitting process [11–14]. Until now, there are only a few investigations about the g-C_3N_4-based nanostructures for the CO_2 photoreduction [15,16]. In our previous work, we have successfully developed Pt-decorated g-C_3N_4 via an environmentally friendly polyol approach and sandwich-like graphene-g-C_3N_4 hybrid nanostructures through a one-pot impregnation-thermal reduction process with excellent performance in the reduction of CO_2 to CH_4 under visible light irradiation [15,16].

To date, in the g-C_3N_4-based system, the ability in light harvesting and photocatalytic performance are still limited. To circumvent the problems, silver halide AgX (X = Cl and Br) is known to be a photosensitive material and it is widely used in the photocatalytic field [17–19]. Coupling of g-C_3N_4 with AgX has been previously reported. For example, Xu et al. [17] developed AgX/g-C_3N_4 hybrid materials by a facile water bath process. In addition, Xu et al. [20] and Yang et al. [21] reported the AgBr/g-C_3N_4 photocatalysts synthesized by deposition-precipitation method. All the developed AgX/g-C_3N_4 photocatalysts were applied for the degradation of organic dyes and displayed outstanding performance than that of individual AgX or g-C_3N_4. However, to the best of our knowledge, no research on the photocatalytic reduction of CO_2 to CH_4 using AgX/g-C_3N_4 nanocomposites has been reported. The charge transfer mechanism of the CO_2 photoreduction over AgX/g-C_3N_4 nanocomposites remains unclear till now. Also, less emphasis is placed on understanding the influence of different types of silver halides (AgX) coupled with g-C_3N_4 in regards to the band potentials and photocatalytic activity. As a result, the emerging role of halide ions (X = Cl and Br) on the photocatalytic activity needs to be further examined and documented.

In order to combine the intriguing properties of the g-C_3N_4 and AgX, herein we reported a facile sonication-assisted deposition-precipitation approach at room temperature to develop AgX/protonated g-C_3N_4 (AgX/pCN) hybrid photocatalysts. The photocatalytic performance was evaluated by performing the CO_2 reduction to CH_4. In this study, two different halide ions (Cl^- and Br^-) on the photoactivity were studied and the relationship between the structural characteristics of AgX/pCN and the photocatalytic reaction was critically discussed. The optimized loading of AgBr improved the CO_2 reduction activity of g-C_3N_4 to a certain extent as compared to that of AgCl. The enhanced photocatalytic activity was attributed to the synergistic interaction between AgBr and pCN with suitable VB and CB edges to facilitate effective charge transfer and separation. Furthermore, upon the light irradiation, the formation of metallic Ag on the AgX surface deposited on pCN is expected to play an indispensable role in the synergistic photocatalytic enhancement due the surface plasmon resonance (SPR) effect. As a whole, this work not only utilizes g-C_3N_4 as an ideal support for solar energy conversion, but also highlights the rational

importance of hybridizing two semiconductors with proper band edge alignments for efficient interfacial charge transfer to suppress the recombination rate of electron–hole pairs. It is anticipated that this study will provide new platforms in the design and development of next generation plasmon-based hybrid heterostructured photocatalysts with high activity and remarkable charge transfer efficiency for realizing a revolution of clean and renewable energy.

2. Experimental

2.1. Synthesis and chemical refinement of g-C_3N_4

All chemical reagents were of analytical grade and used without further purification. Deionized (DI) water (>18.2 MΩ cm resistivity) was employed in the experiment. Bulk g-C_3N_4 was synthesized based on our previous reported thermal polymerization approach [15,16,22]. Briefly, 3 g of urea was put into a ceramic crucible with a cover. The crucible was heated at 520 °C for 2.5 h at a heating rate of 10 °C min^{-1}. The yielded light yellow product was ground into powder form. This was followed by the chemical refinement and protonation of the developed g-C_3N_4 as reported in our recent published communication [22]. Specifically, 1 g of the bulk g-C_3N_4 was ultrasonically treated for 1 h in 200 mL of 0.5 mol L^{-1} HCl aqueous solution. After sonication treatment, the exfoliated g-C_3N_4 in the acid suspension was further stirred magnetically at room temperature for 4 h. Finally, the mixture was constantly washed with DI water to remove excess HCl until the pH of the filtrate water became neutral and then dried at 70 °C for 12 h. The protonated g-C_3N_4 was denoted as pCN.

2.2. Development of AgX/pCN (X = Cl and Br) hybrid photocatalysts

The AgX/pCN samples were prepared via a sonication-assisted deposition-precipitation technique. Typically, 0.5 g of the as-obtained pCN was added into 50 mL of DI water and sonicated for 30 min. Next, a solution of $AgNO_3$ with a concentration of 0.01 g/mL was added drop wise to the suspension. The mixture was stirred magnetically for 1 h to allow adsorption of Ag^+ ions on the surface of pCN. Then, the respective aqueous solutions of sodium halides NaX (X = Cl and Br) were added dropwise into the suspension with an excess amount of 10% to ensure that the amount of halide ions from NaX was more than adequate to precipitate Ag^+ on the g-C_3N_4 surface. The dropwise addition of NaX was necessary to avoid rapid nucleation process of the Ag^+ and X^- on the pCN in the solution. The resulting mixture was further stirred vigorously at room temperature for 3 h. The product was obtained by washing with ethanol and DI water for three times and then dried at 70 °C for 12 h. Following this facile method, a series of AgX/pCN with different mass ratio of $AgNO_3$ to pCN(10%, 30%, 50% and 70%) was developed. The samples were denoted as yAgX/pCN where y = 10, 30, 50 and 70, and X represented Cl or Br. Upon the light irradiation, the formation of Ag on the surface of AgX due to its photoreduction process was observed during the catalytic reactions. The spent photocatalysts were known as Ag/AgX/pCN after the end of reaction. For comparison, pure AgCl and AgBr crystals fabricated without the incorporation of pCN were also prepared under the similar experimental conditions. Also, a physically mixed AgBr and pCN with the similar loading of AgBr as the 30AgBr/pCN sample (denoted as 30AgBr/pCN-M) was synthesized by grinding both AgBr and g-C_3N_4 in an agate mortar for 15 min.

2.3. Catalyst characterization

Zeta potential measurements were performed using the Zetasizer Nano ZS (Malvern Instruments) based on the dynamic

light-scattering analysis. Prior to the analysis, 20 mg of the sample was placed in 50 mL of DI water followed by sonication for 15 min at room temperature. The surface morphology of the as-synthesized samples was analyzed using field emission scanning electron microscopy (FESEM) (Hitachi SU8010) equipped with an Oxford-Horiba Inca XMax 50 energy dispersive X-ray (EDX) and transmission electron microscopy (TEM) (JEOL JEM-2100F). The TEM images were obtained at an accelerating voltage of 200 kV. The crystallographic structure was investigated using powder X-ray diffraction (XRD) (Bruker D8 Discover X-ray Diffractometer) using Cu Kα radiation (λ = 0.154056 nm) with a Ni filter operated at 40 kV and 40 mA. The XRD patterns were collected in the diffraction angle (2θ) ranging from 5 to 90° at a scan rate of 0.02° s^{-1}. The Fourier transform infrared (FTIR) spectra of the samples were performed using Thermo-Nicolet iS10 spectrometer at room temperature using a standard KBr pellet method with a resolution of 4 cm^{-1} in the range of 4000–400 cm^{-1}. The absorption spectra of the samples were measured by a Cary 100 Ultraviolet-visible (UV–vis) spectrophotometer equipped with an integrated sphere using BaSO$_4$ as a reference standard. The X-ray photoelectron spectroscopy (XPS) analysis was carried out with a Kratos Axis-Ultra DLD instrument using the Al Kα X-ray radiation (1486.6 eV) operated at 200 W and a pass energy of 20 eV under the ultra-vacuum environment (7.6×10^{-9} Torr). All the binding energies were calibrated with the C 1s peak at 284.6 eV based on the adventitious carbon. The XPS spectra were acquired using the vision software, comprising both vision processing and vision manager. High resolution XPS peaks were deconvoluted by means of Gaussian–Lorentzian functions after a Shirley background subtraction. The photoluminescence (PL) spectra were evaluated by a 325 nm He-Cd laser as the excitation light source at room temperature using Renishaw in Via Raman Microscope. The PL emission spectra were measured from 350 to 750 nm.

2.4. Evaluation of photocatalytic activity

The reduction of CO$_2$ was conducted in a homemade, continuous gas-phase photoreactor at ambient temperature and atmospheric pressure as described in our previous communications [5,15,16,23,24]. A low-power 15 W energy-saving daylight lamp (Model: Philips, TORNADO 15 W WW E27 220–240 V 1CT) was utilized and its light spectrum was shown in the previous works [5,23,25]. High purity of CO$_2$ (99.99%) was passed through a water bubbler to form a mixture of water vapor and CO$_2$. Before turning on the light source, a flow rate of 5 mL/min of wet CO$_2$ measured using a mass flow controller was purged in the reactor for 30 min, which was loaded with coated photocatalysts of 100 mg. This was aimed to evacuate the air in the reactor system and simultaneously to attain complete adsorption of gas molecules on the catalyst surface. The light was switched on after 30 min of purging. A thermometer attached to a digital temperature reader was used to closely monitor the temperature in the system. The accumulated light intensity of 8.5 mW cm^{-2} was measured using a pyranometer (Kipp and Zonen type CMP 6) with a distance of 5 cm from the light source to the reactor. The concentration of product gas was determined by a gas chromatography (GC) (Agilent 7890A, Hayesep Q and mol sieve column) equipped with both flame ionized detector (FID) and thermal conductivity detector (TCD). The concentration of CH$_4$ was measured based on the peak area of the GC spectrum by employing the standard reference technique. The reactor was placed in a black box to avoid the light interference from the surroundings. The reactions were performed at least twice under similar experimental conditions to ensure the reproducibility of the photocatalysts. Consistent results with percentage errors less than 5% were achieved in all cases. Four consecutive cycles of reaction were carried out to determine the stability of the photocatalyst. The total CH$_4$ evolu-

tion after 10 h of reaction was calculated using Eq. (1). To verify the visible-light-activity of the optimized photocatalyst, the photoreduction of CO$_2$ experiment was conducted under the irradiation of a 500 W Xenon arc lamp (Model no.: CHF XM500 W) equipped with a UV cut-off filter to remove UV light ($\lambda > 400$ nm) for 10 h as shown in Figs. S5 and S6 in Supplementary material.

$$\text{Total CH}_4 \text{ evolution} = \frac{\text{total amount of CH}_4 \text{ produced } (\mu\text{mol})}{\text{amount of photocatalyst used (g – catalyst)}}$$
(1)

3. Results and discussion

3.1. Synthesis approach

The protonation of g-C$_3$N$_4$ could be evidenced by the zeta potential analysis in which the surface charge of g-C$_3$N$_4$ was modified from −15.4 to +14.0 mV (Fig. S1 in Supplementary material), implying successful protonation by HCl. Prior to the addition of AgNO$_3$ and NaX, pCN underwent sonication to delaminate stacked layers of pCN. The presence of abundant amine groups served as a good ligand (Lewis base) for Ag$^+$, resulting in a strong coordination between Ag$^+$ and pCN [20,26]. This was followed by the formation of AgX (X = Cl and Br) nanocrystals through in situ nucleation mechanism by a deposition-precipitation method at room temperature. The synthesis routes of the formation of AgX/pCN hybrid nanocomposites were depicted in Fig. 1.

3.2. Material characterization

To study the microscopic and structural morphology of pure AgX and AgX/pCN samples, FESEM and TEM analyses were performed. From Fig. 2a and b, the morphologies of pure AgBr and AgCl were of irregular spheres with diameters ranging from 1 to 3 μm. Upon the incorporation of pCNas a support, all AgX crystals ripened to form nanoparticles on the pCN surface (Fig. 2c–h). This clearly showed that pCN acted as a nucleation site to reduce the agglomeration of AgX [18,27]. Moreover, AgX crystals exhibited a nano-sized structure on the pCN surface. Evidently, the average particle sizes of pure AgBr crystals and 30AgBr/pCN hybrid nanocomposites reduced drastically from 1689 to 44 nm (insets of Fig. 2a and d). In comparison to AgCl and 30AgCl/pCN, the mean diameters were found to be 1886 and 58 nm, respectively (insets of Fig. 2b and h). It is expected that the formation of nanocrystals is integral for the enhancement of CO$_2$ reduction to favor more reactive sites. Additionally, AgBr/pCN with various loadings of AgBr was used as a representative model to demonstrate the AgX/pCN nanocomposites. It could be observed from Fig. 2c–f that increasing loading of AgBr on the pCN led to an increase in the particle size and more clumps due to the agglomeration of AgBr particles. The elemental mapping by EDX analysis showed that the C, N, Ag, Br and Cl elements were detected in the AgBr/pCN and AgCl/pCN samples with all elements distributed over the hybrid nanocomposites (Fig. 3).

The XRD patterns of the as-developed AgX/pCN with various loadings of AgX were depicted in Fig. 4. The XRD pattern of pCN was almost similar to that of pure g-C$_3$N$_4$ with a pronounced peak at 27.2° ascribed to the (0 0 2) diffraction plane of a graphitic structure at an interlayer distance of 0.325 nm, implying that g-C$_3$N$_4$ was made up of densely stacked layers [16]. In addition, a peak at 13° corresponding to a distance of 0.675 nm represented the in-plane structural packing motif of tri-s-triazine units (JCPDS 087-1526) [28]. This claimed that the original nature of g-C$_3$N$_4$ in the pCN upon chemical refinement by HCl was well-preserved.
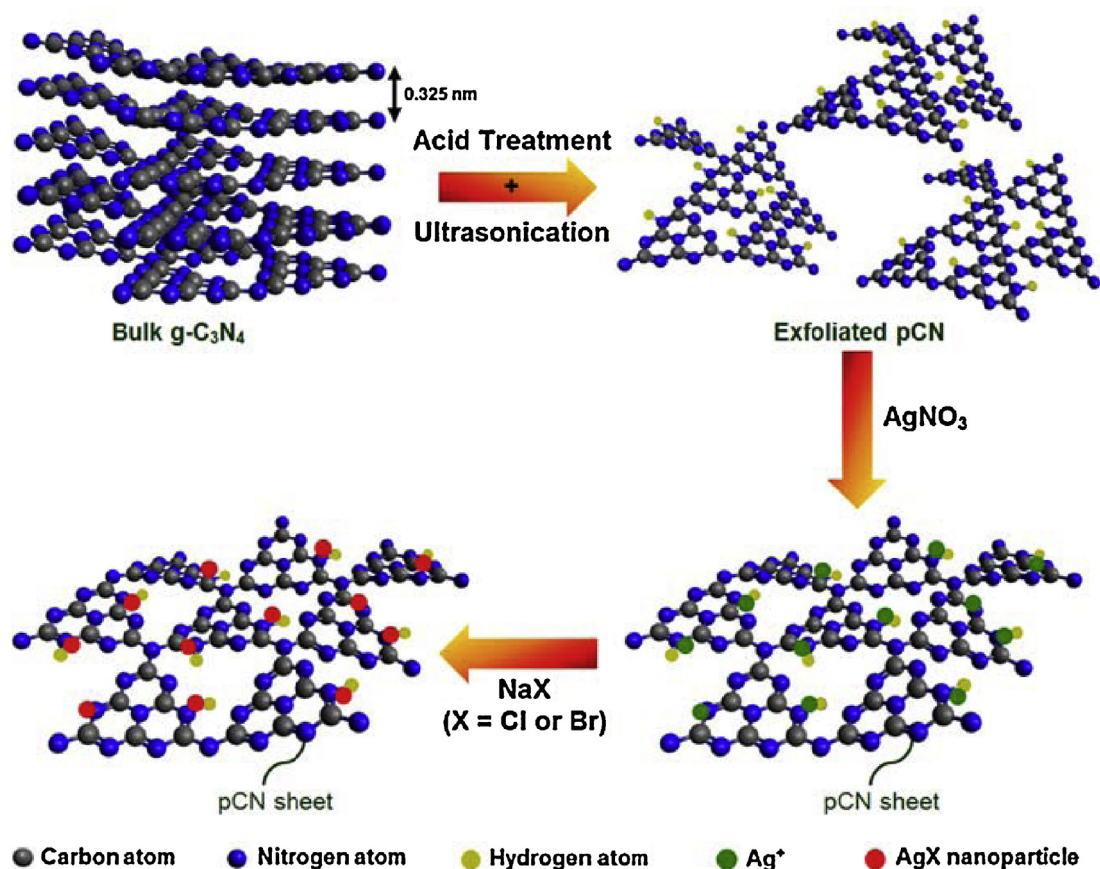
Fig. 1. Synthesis strategy of the AgX/pCN hybrid nanocomposites via a sonication-assisted deposition-precipitation technique.

As for the AgX/pCN nanocomposites, both AgBr/pCN and AgCl/pCN samples followed similar trends: with increasing AgX loadings from 10% to 70%, the characteristic peaks of g-C_3N_4 became weaker and the intensities of AgX peaks were more prominent. The as-prepared AgBr/pCN hybrid nanocomposites were predominantly AgBr cubic phase. The diffraction peaks at 2θ values of 26.8°, 30.8°, 44.2°, 52.6°, 55.1°, 64.5° and 73.2° were well-indexed to the (1 1 1), (2 0 0), (2 2 0), (3 1 1), (2 2 2), (4 0 0) and (4 2 0) lattice planes of AgBr cubic crystal (Fig. 4A), respectively (JCPDS 06-0438) [18,21]. On the other hand, the diffraction peaks of AgCl/pCN at 27.8°, 32.2°, 46.2°, 54.8°, 57.5°, 67.5° 74.5° and 76.8°corresponded to the (1 1 1), (2 0 0), (2 2 0), (3 1 1), (2 2 2), (4 0 0), (3 3 1) and (4 2 0) lattice planes of AgCl cubic crystal phase (Fig. 4B), respectively (JCPDS 31-1238) [29]. It was noticed that no diffraction peaks of g-C_3N_4 were found with AgX loadings more than 50% owing to the comparatively lower content of pCN. No clear diffraction peaks of metallic Ag and other impurities were detected in both AgBr/pCN and AgCl/pCN samples, indicating that a high purity of g-C_3N_4 and AgX was obtained.

The FTIR spectra of pure g-C_3N_4, pCN and AgX/pCN samples were illustrated in Fig. 5 and S2 (Supplementary material). For pCN sample, the absorption bands were almost similar to that of pure g-C_3N_4 reported in our previous works [15,28], implying that chemical refinement from the acid pretreatment process did not markedly affect the atomic structures of pure g-C_3N_4. Evidently, the strong absorption peaks in the region of 1200–1650 cm^{-1}, centered at 1635, 1572, 1416, 1325 and 1249 cm^{-1}, were attributed to the typical stretching vibration of C—N and C=N heterocycles [30]. Additionally, the breathing mode of tri-s-triazine units was observed at 812 cm^{-1}. In the case of AgX/pCN nanocomposites, it was noticed that the main peaks of g-C_3N_4 in the 1200–1650 cm^{-1}

were still present without distinct blue shift or red shift upon the hybridization of AgX nanoparticles. Interestingly, the characteristic band of tri-s-triazine ring was slightly red shifted from 812 to ca. 807 cm^{-1} (Fig. 5B), revealing that interactions were formed between the "nitrogen pots" of pCN and Ag species of AgBr. This phenomenon was in accordance with a recent report on SnS$_2$/g-C_3N_4 nanocomposites by Zhang et al. [31].

The chemical composition and bonding configuration of the as-prepared pCN, 30AgBr/pCN and 30AgCl/pCN were characterized by XPS analysis (Fig. 6). As shown in the survey XPS spectra (Fig. 6a), all the samples were composed of C, N and O elements. A small amount of oxygen was ascribed to the adsorption of oxygen from the atmosphere during the preparation, which was consistent with the reported literatures [32,33]. In addition to C, N and O elements, the presence of Ag 3p, Ag 3d, Br 3p, Br 3d and Br 3s was detected from the 30AgBr/pCN sample. Meanwhile, for 30AgCl/pCN sample, the peaks of Ag 3p, Ag 3d, Cl 2p and Cl 2s were observed. Based on Fig. 6b, the high resolution C 1s spectra could be deconvoluted into three peaks centered at ca. 284.6, 286.0 and 288.1 eV, being attributed to the standard reference sp^2 graphitic carbon (C—C bonding), sp^2-bonded in the s-triazine units (N—C=N) and sp^3-hybridized carbon atoms (C—(N)$_3$) in the g-C_3N_4 lattice, respectively [34,35]. In addition, four fitted peaks located at binding energies of ca. 398.6, 400.0, 401.1 and 404.2 eV were observed in the high resolution N 1s spectra (Fig. 6c). The dominant peak at ca. 398.6 eV corresponded to the sp^2-bonded nitrogen (pyridine-N) in the triazine rings (C—N=C) [36]. The C—N=C served as the main carbon and nitrogen elements in the skeleton, which was regarded as the building block of the conjugated system. The emerging peak at ca. 400.0 eV belonged to the tertiary nitrogen bonded to carbon atoms (pyrrolic-N) in the form of N—(C)$_3$ [37]. Both pyridine-N and
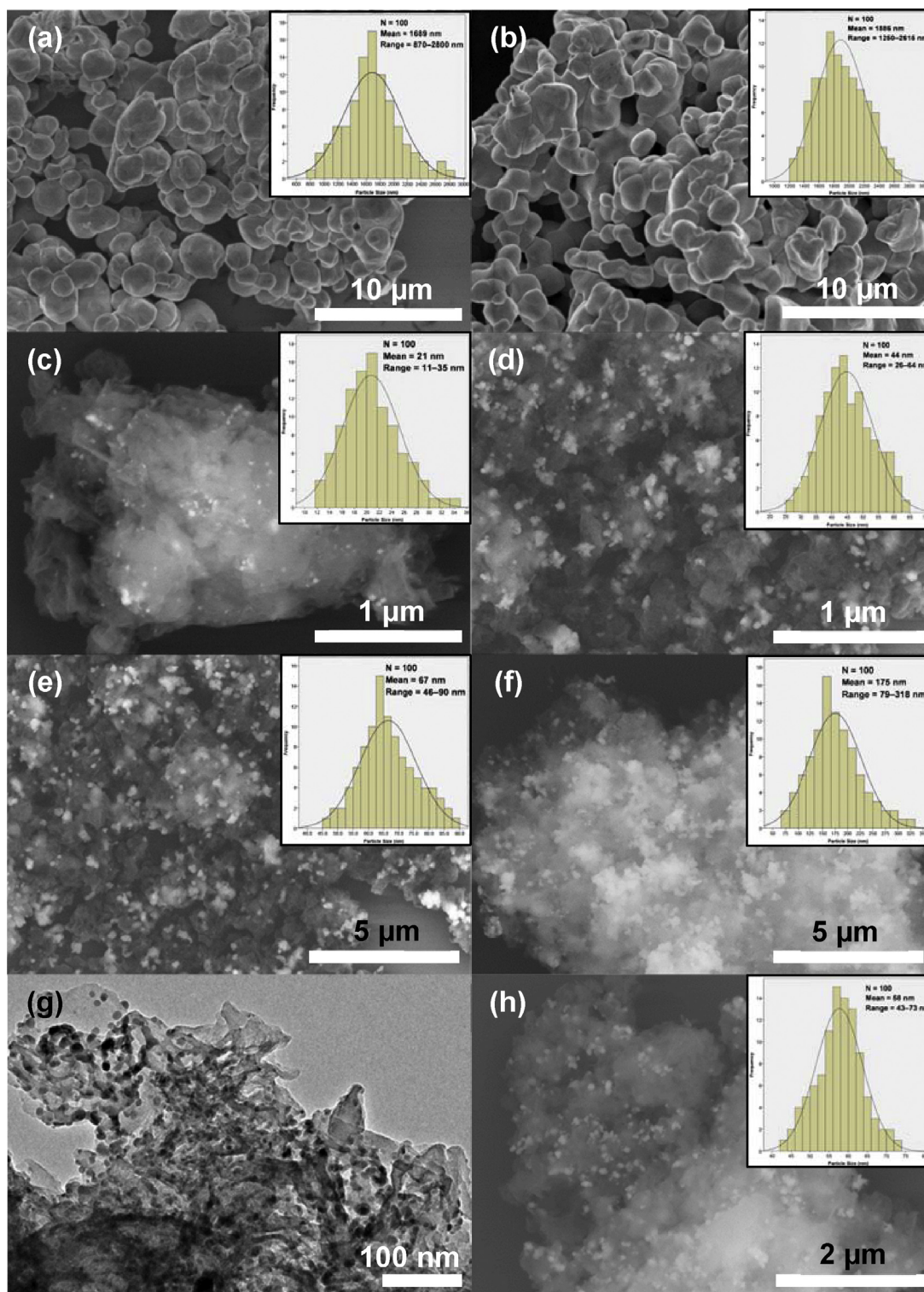
Fig. 2. FESEM images of (a) pure AgBr, (b) pure AgCl, (c) 10AgBr/pCN, (d) 30AgBr/pCN, (e) 50AgBr/pCN and (f) 70AgBr/pCN hybrid nanocomposites. (g) TEM image of 30AgBr/pCN sample. (h) FESEM image of 30AgCl/pCN sample. Insets of (a)–(f) and (h) show the particle size distribution of AgX.

pyrrolic-N along with N—C=N formed the heptazine heterocyclic ring units, which were the elementary substructure of g-C$_3$N$_4$. The peak at ca. 401.1 eV was assigned to the presence of amino groups (graphitic-N, C—N—H) [38]. The contribution at 404.2 eV was originated from the positive charge effect in the heterocycles owing to the protonation of g-C$_3$N$_4$ [39]. Interestingly, after the deposition of AgX on the pCN, the binding energies of both pyrrolic-N and graphitic-N in the AgX/pCN samples shifted to lower and higher

binding energies, respectively. From the literature, a slight shift in the binding energy can be inferred by the electron transfer and interfacial interaction between pCN and AgX as a result of different electron concentration, forming a hybrid heterojunction. This was concordant with other reported hybrid nanomaterials such as TiO$_2$/g-C$_3$N$_4$ and CdS/g-C$_3$N$_4$ [40,41]. The high resolution Ag 3d spectra were delineated in Fig. 6d. The peaks of Ag 3d were positioned at binding energies of ca. 367.6 and 373.6 eV, which were
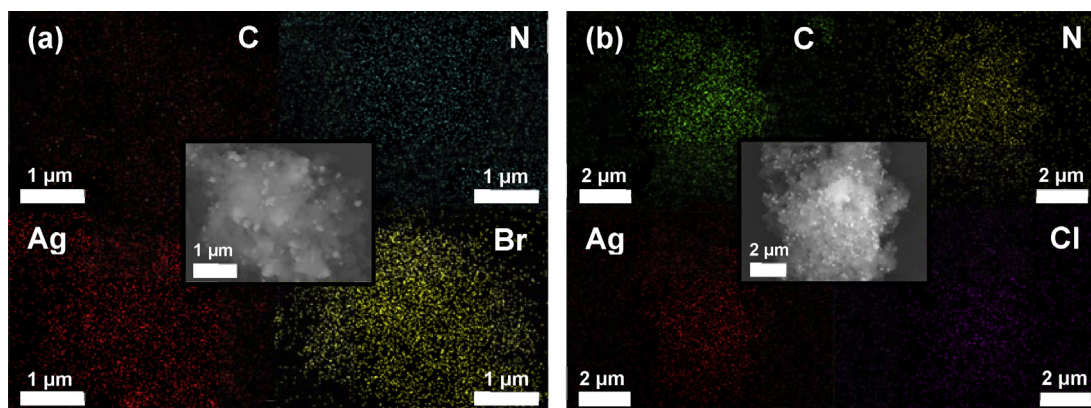
Fig. 3. EDX mapping of C, N, Ag, Br and Cl elements for (a) AgBr/pCN and (b) AgCl/pCN samples. Insets of (a) and (b) show the corresponding FESEM images of AgBr/pCN and AgCl/pCN samples for elemental mapping.
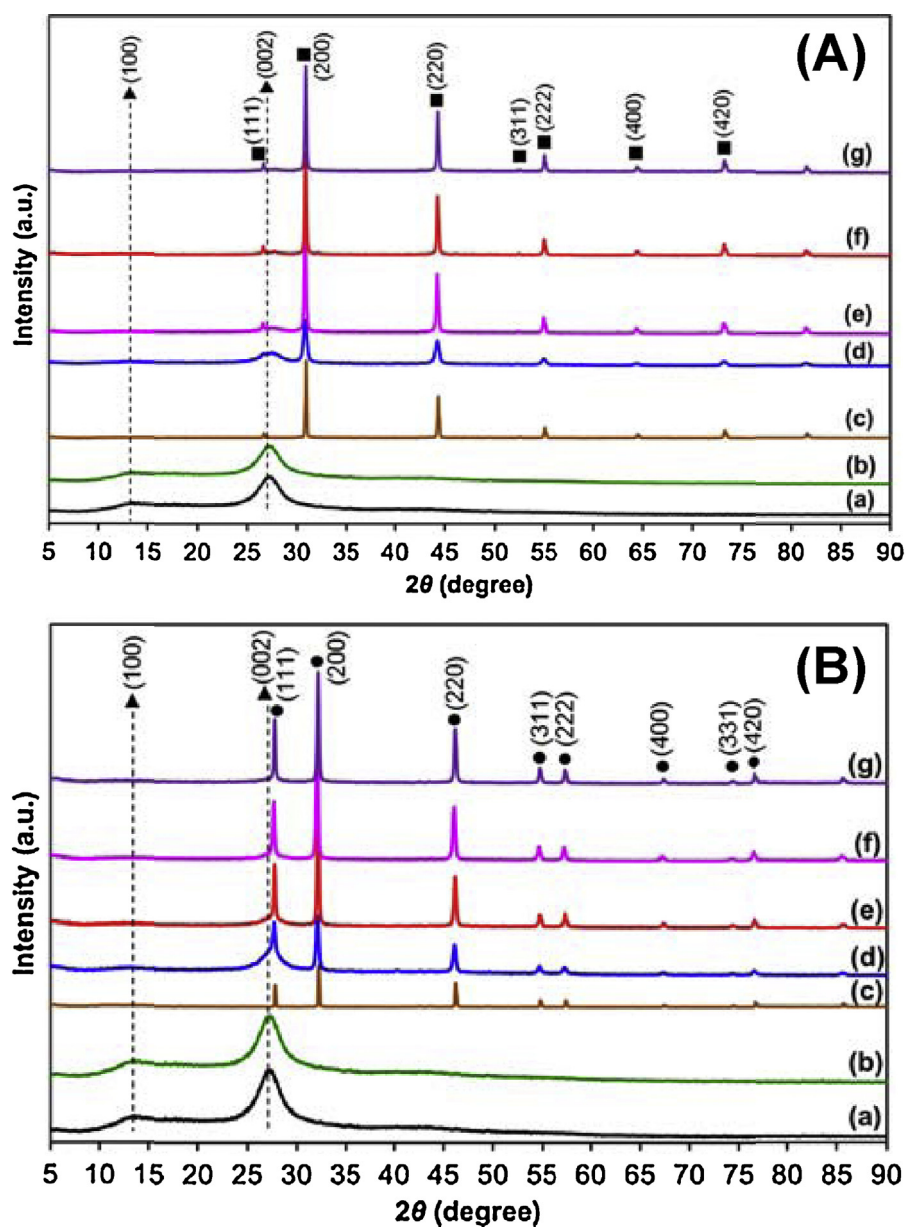

Fig. 4. XRD patterns of (A) AgBr/pCN ((a) pure g-C₃N₄, (b) pCN, (c) pure AgBr, and (d–g) 10%, 30%, 50% and 70% of AgBr) and (B) AgCl/pCN ((a) pure g-C₃N₄, (b) pCN, (c) pure AgCl, and (d–g) 10%, 30%, 50% and 70% of AgCl) hybrid nanocomposites. Triangle, square and circle symbols represent the reflections of g-C₃N₄, AgBr and AgCl, respectively.
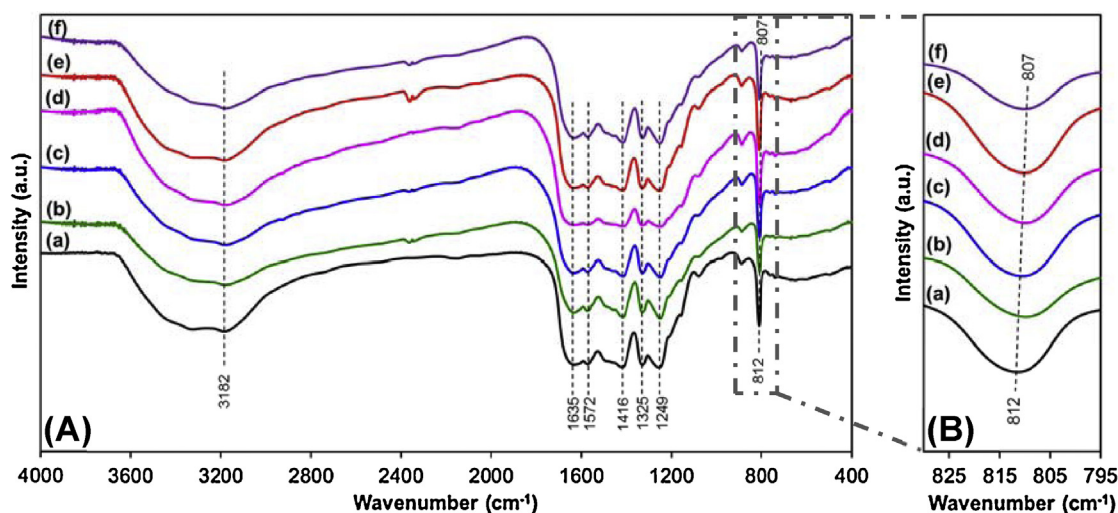
Fig. 5. (A) FTIR spectra of (a) pure g-C_3N_4, (b) pCN, (c) 10AgBr/pCN, (d) 30AgBr/pCN, (e) 50AgBr/pCN and (f) 70AgBr/pCN nanocomposites. (B) Enlarged FTIR spectra corresponding to the dotted rectangle from the image (A).

accredited to the Ag $3d_{5/2}$ and Ag $3d_{3/2}$, respectively. Particularly, the two peaks centered at 367.6 and 373.6 eV belonged to Ag$^+$ ions of AgBr and AgCl, whereas another pair of peaks located at ca. 368.6 and 374.3 eV was assigned to the metallic Ag^o species. Similar results were also reported by other researchers [42]. In this case, the presence of metallic Ag^o was due to the photocorrosion of the sample during the XPS analysis since AgX is a highly photosensitive material. Similarly, two individual peaks at 68.1 and 69.1 eV correlated well with the Br $3d_{5/2}$ and Br $3d_{3/2}$ (Fig. 6e), showing the existence of Br$^-$ [18]. On top of that, the double peaks of Cl $2p_{3/2}$ and Cl $2p_{1/2}$ with binding energies of 197.7 and 199.5 eV, respectively, were shown in Fig. 6f, implying the presence of Cl$^-$. As a whole, the XPS data further confirmed the successful synthesis of AgX/pCN hybrid heterostructures, which was in agreement with the FESEM, TEM, XRD and FTIR results.

The UV–vis absorption spectra of the as-developed pCN, AgBr/pCN and AgCl/pCN samples were displayed in Fig. 7. The pCN sample demonstrated an absorption edge at ca. 440 nm, which was similar to that of pure g-C_3N_4. The band gap energy of both samples was estimated to be 2.8 eV, which coincided well with the reported literatures [30,43,44]. Surprisingly, with the incorporation of AgX nanoparticles on pCN, the absorption edge of AgX/pCN did not vary notably. The absorption intensities of AgX/pCN in the visible light region were slightly improved with increasing AgX loadings, which were in concord with the color changing from light yellow to gray (inset of Fig. 7). Meanwhile, the absorption edge of pure AgBr was found to be ca. 480 nm, corresponding to the band gap energy of 2.6 eV. In comparison to pure AgBr, the band gap energy of pure AgCl was larger (3.2 eV) (Fig. S3 in Supplementary material). As a result, pure AgBr and AgBr/pCN photocatalysts could absorb more visible light as compared to those of AgCl and AgCl/pCN photocatalysts. Therefore, the improved visible light absorption of AgBr/pCN over AgCl/pCN nanocomposites is anticipated to produce more electron-hole pairs, resulting in a higher photocatalytic performance. This postulation was confirmed by performing the CO_2 photoreduction under visible light irradiation at ambient conditions.

3.3. Photocatalytic activity and mechanism of photocatalytic enhancement

The photocatalytic reduction of CO_2 to CH_4 in the presence of water vapor was performed at ambient conditions under a low-power 15 W energy-saving daylight bulb. A series of control experiments was performed such as (1) in the dark, (2) without

photocatalysts, (3) without H_2O vapor and (4) under the flow of N_2 and H_2O vapor. It was found that no considerable evolution of CH_4 was detected in all cases (Fig. S4 in Supplementary material), signifying that catalysts, light and water vapor were essential for the CO_2 reduction to CH_4. Importantly, when CO_2 was replaced with N_2 gas, there was no detectable CH_4 product, claiming that CH_4 was not evolved from the decomposition of pCN. Thus, this proved that the evolution of CH_4 was originated from the photocatalytic reduction of CO_2 with H_2O in the presence of light.

As indicated in Fig. 8, the incorporation of AgX on the pCN plays a significant influence on the photocatalytic reduction of CO_2. In the absence of AgX, pure g-C_3N_4 exhibited a low CH_4 evolution of 2.55 μmol $g_{catalyst}^{-1}$ due to the rapid recombination of charge carriers. The pCN showed similar photoactivity to the pure g-C_3N_4, attaining a total CH_4 evolution of 2.58 μmol $g_{catalyst}^{-1}$. By hybridizing AgBr with pCN, the photocatalytic activity of 30AgBr/pCN hybrid heterostructure was the highest as compared to other AgBr/pCN samples, achieving a maximum CH_4 evolution of 10.92 μmol $g_{catalyst}^{-1}$. This exemplified a walloping 34.1- and 4.2-fold enhancement in the CH_4 production over bare AgBr and pCN, respectively. Undoubtedly, there exists an optimal AgX content on the pCN surface to obtain the maximum photoactivity, which is basically similar to any dopants or co-catalysts such as metal, non-metal or metal oxide [31,45,46]. In this work, when the loading of AgBr exceeded 30%, the total CH_4 evolution was deteriorated as shown in the 50AgBr/pCN (9.52 μmol $g_{catalyst}^{-1}$) and 70AgBr/pCN samples (8.62 μmol $g_{catalyst}^{-1}$). This was attributed to the fact that excessive AgBr loading caused a severe aggregation on the pCN surface.

From the GC analysis, the sole hydrocarbon product from the photoreduction of CO_2 was CH_4. The formation of products is related to the band potentials of the photocatalyst and the redox potentials of the reaction products [32]. The CB potential of pCN was found to be −1.15 eV vs. NHE, while the reduction potentials of the possible products were: CO_2/CH_4: −0.24 V [47]; CO_2/CH_3OH: −0.38 V [1]; CO_2/CO: −0.52 V [48]; $CO_2/HCOOH$: −0.61 V [49]. Since the reduction potential for the CH_4 evolution was lower than that required for HCOOH, CO and CH_3OH, CO_2 was preferably reduced to CH_4 over the AgX/pCN samples. Furthermore, H_2 molecules were not identified by GC. This was possibly because the photogenerated •H radicals and H_2 were competitively consumed by CO_2 in the reaction. Similar observation has also been reported by Liu et al. [50], Yu et al. [51], Wang et al. [52] and also in our previous published works [5,15,16,22–24,53].
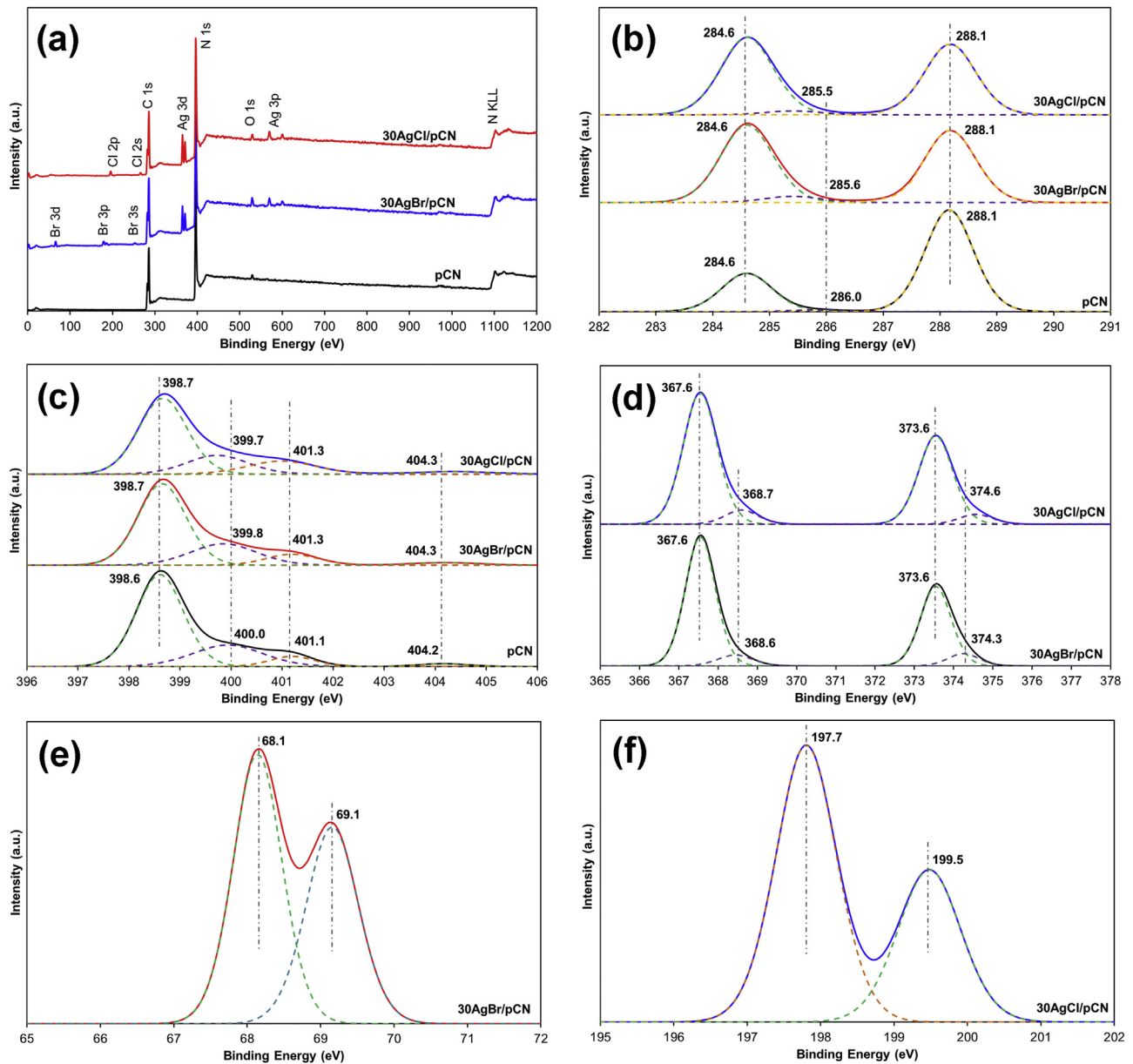
Fig. 6. (a) XPS survey spectra of the pCN, 30AgBr/pCN and 30AgCl/pCN photocatalysts. High resolution XPS spectra of (b) C 1s, (c) N 1s, (d) Ag 3d, (e) Br 3d and (f) Cl 2p of pCN, 30AgBr/pCN and 30AgCl/pCN samples.
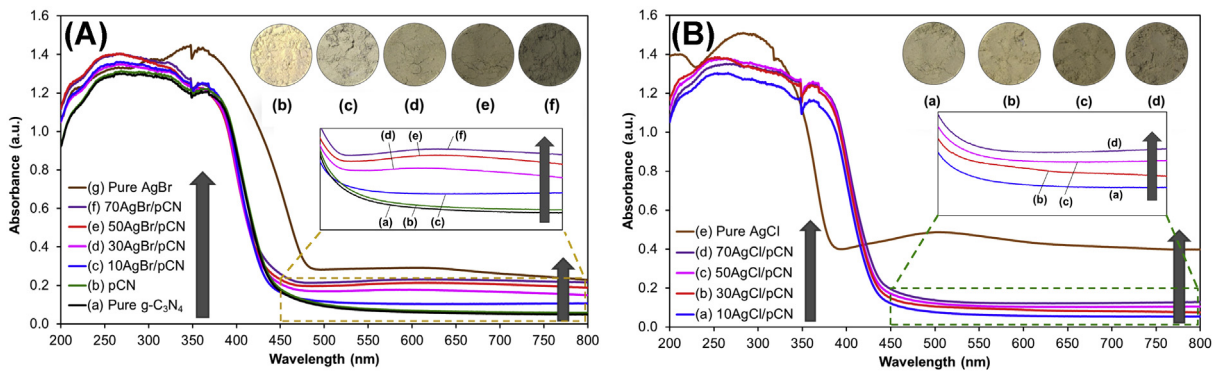

Fig. 7. UV–vis absorption spectra of the as-synthesized samples: (A) AgBr/pCN and (B) AgCl/pCN hybrid heterostructures. Insets of (A) and (B) show the digital photographs and the enlarged region of visible light absorption of the samples.
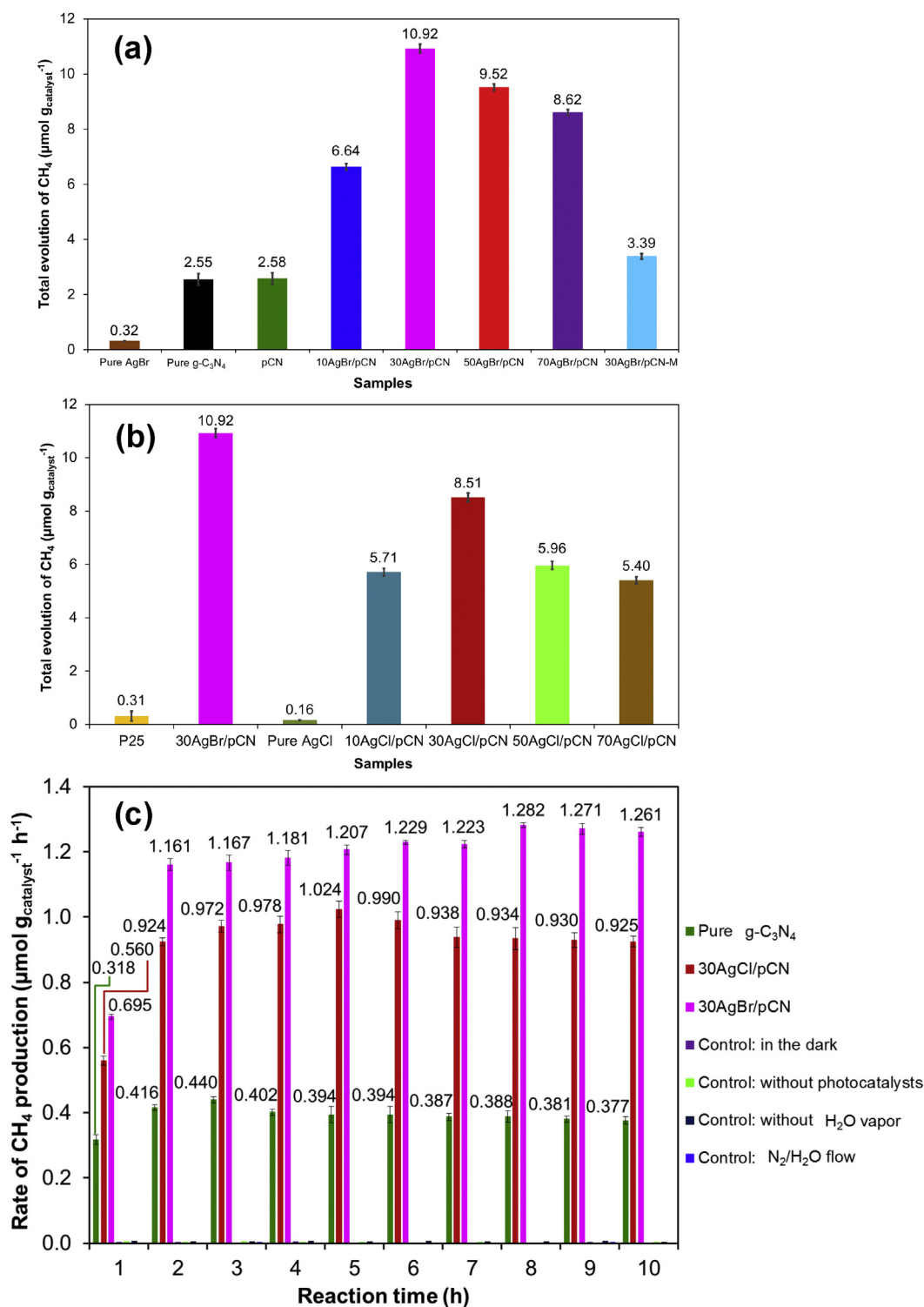
Fig. 8. (a–b) Total production of CH_4 from the CO_2 photoreduction over pure g-C_3N_4, AgBr/pCN and AgCl/pCN hybrid nanocomposites. (c) Time dependence of the rate of CH_4 production over pure g-C_3N_4, 30AgBr/pCN and 30AgCl/pCN samples.

In order to further examine the interfacial contact between AgBr and pCN as well as the separation efficiency of pho-togenerated electron-hole pairs in the AgBr/pCN samples, PL analysis was conducted as divulged in Fig. 9A. The PL emission intensity followed the order: pCN> 10AgBr/pCN> 70AgBr/pCN> 50AgBr/pCN> 30AgBr/pCN. The sequence in the degree of PL intensity agreed well with our photocatalytic results of AgBr/pCN samples. Among all the samples, the 30AgBr/pCN

sample manifested the most diminished PL intensity, accentuating that it had the most effective inhibition of recombination of electron-hole pairs in the hybrid system. This was benefitted from the synergistic efficient shuttling of charge carriers between pCN and AgBr at the optimum loading across the heterojunction interface to retard the recombination process.

Additionally, to validate the formation of intimate heterojunc-tion interface of AgBr/pCN for the improved photocatalytic activity,
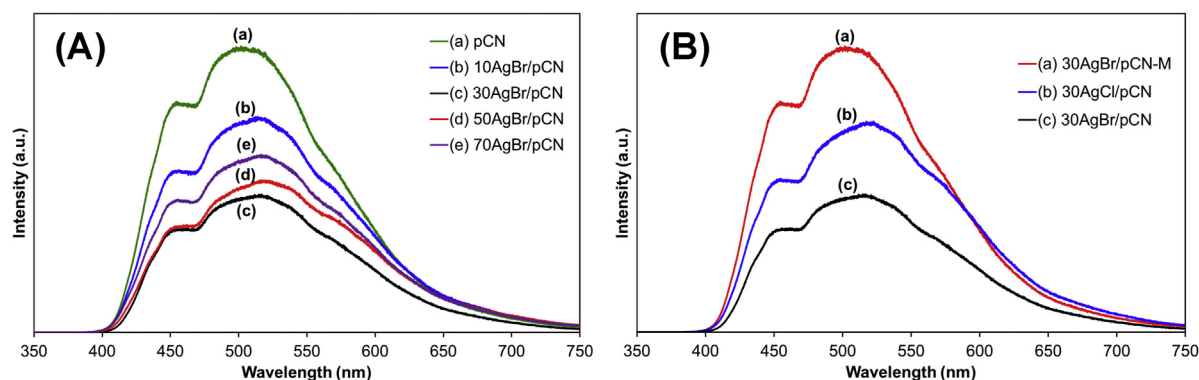
Fig. 9. (A) PL spectra of pCN and AgBr/pCN hybrid heterostructures. (B) PL spectra of 30AgBr/pCN, 30AgBr/pCN-M and 30AgCl/pCN samples.
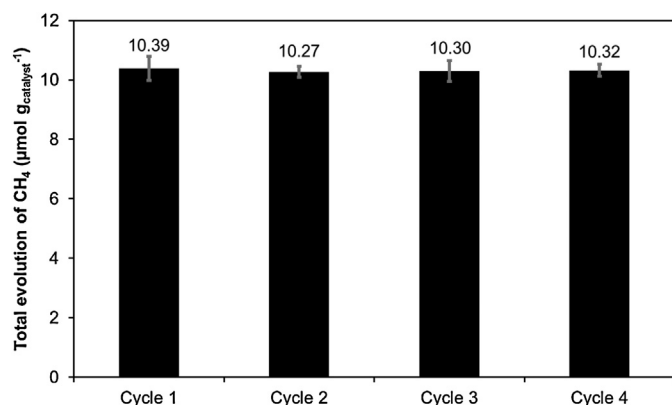

Fig. 10. Recycle test for the photoreduction of CO_2 to CH_4 in the presence of 30AgBr/pCN photocatalysts under the light irradiation.

a physically mixed 30AgBr/pCN-M sample was tested for the CO_2 reduction to CH_4. Referring to Fig. 8a, the 30AgBr/pCN-M demonstrated a much lower total CH_4 generation (3.39 μmol $g_{catalyst}^{-1}$) than that of 30AgBr/pCN (10.92 μmol $g_{catalyst}^{-1}$) despite exhibiting similar mass ratio of AgBr in both samples. This clearly revealed the significance of well-developed coupling heterojunction interface between pCN and AgBr for efficient charge transfer and separation. This observation could also be corroborated by the PL spectra (Fig. 9B), where the PL emission peak of 30AgBr/pCN was lower than that of 30AgBr/pCN-M, which was in accordance with our photocatalytic results. Hence, it can be concluded that the effective photoinduced charge transfer across the well interconnection of heterojunction is of utmost importance for the enhanced photoactivity of AgBr/pCN photocatalysts.

To examine the photostability and recyclability of the photocatalyst, 30AgBr/pCN was employed as a representative sample to conduct four successive photocatalytic reactions (total duration of 40 h). As illustrated in Fig. 10, the 30AgBr/pCN sample maintained its high catalytic activity toward the CO_2 photoreduction process without a significant reduction in the CH_4 evolution after four successive cycles under identical experimental conditions, signifying a high photostability and reusability. After four successive photocatalytic runs, the spent 30Ag/AgBr/pCN and 30Ag/AgCl/pCN photocatalysts were analyzed using XPS analysis (Fig. 11) to check for the presence of metallic Ag^o. Based on Fig. 11c and d (Ag 3d spectra), the intensities of the peaks located at ca. 368.6 and 374.4 eV, which were ascribed to the metallic Ag^o species, were increased after four cycles of reactions in comparison to those before the photocatalytic reactions. This clearly implied that a small amount of AgBr and AgCl was reduced to metallic Ag^o under the irradiation of daylight bulb. As presented in our previous works [5,16,23],

there was a small fraction of UV light (<2%) present in the energy-saving daylight bulb. Therefore, the large band gap of AgCl could still be excited under the daylight bulb, generating charge carriers. Overall, under the illumination of light, AgX (X = Cl and Br) was first excited to produce electrons at the CB of the AgX. The photogenerated electrons from the CB of AgX reacted with Ag^+ to form Ag^o. According to the XPS results, the mole fractions of Ag^o to total Ag were calculated to be 0.26 and 0.38 in the spent 30Ag/AgBr/pCN and 30Ag/AgCl/pCN samples, respectively after the photocatalytic reactions as compared to those of 0.08 and 0.07 in the 30AgBr/pCN and 30AgCl/pCN, respectively before the reactions based on the curve fittings of the Ag 3d region. Furthermore, the decrease in the intensity of the Ag^+ in the Ag 3d (Fig. 11c and d), Br 3d (Fig. 11e) and Cl 2p peaks (Fig. 11f) of the spent samples after photocatalytic reactions also confirmed that the amount of metallic Ag^o became greater, inferring the transformation of some Ag^+ ions to Ag^o during the photocatalytic process.

On top of that, similar photocatalytic trends could also be observed for the AgCl/pCN samples (Fig. 8B). The optimal AgCl loading on the pCN was determined to be 30%. By comparing different halide ions, the total CH_4 evolution of pure AgBr was higher (0.32 μmol $g_{catalyst}^{-1}$) than that of pure AgCl (0.16 μmol $g_{catalyst}^{-1}$). This could be verified by the UV–vis absorption spectra as illustrated in Fig. 7. Since the band gap energy of pure AgBr was measured to be 2.6 eV, which was lower than that of pure AgCl (3.2 eV), this readily rendered a wider range of visible light absorption harvested by AgBr, resulting in a higher catalytic activity. This was also another major reason why the optimal 30AgBr/pCN reported a higher catalytic performance than 30AgCl/pCN. This was due to the ease of photoexcitation of electrons from AgBr in the AgBr/pCN samples upon the light irradiation. Other detailed reasons why 30AgBr/pCN possessed an overwhelmingly better performance in the CH_4 generation as compared to 30AgCl/pCN were systematically discussed as follows:

Based on the XPS analysis as discussed earlier (Fig. 11), the formation of metallic Ag on the surface of AgX plays an influential role in the SPR effect by harvesting the visible light and transforming the plasmonic energy of incoming photons into localized SPR oscillations, thus generating electron–hole pairs [54–56]. When Ag was anchored on the AgX due to photoreduction process upon the light irradiation, a Schottky barrier was created at the interface of Ag/AgX owing to the difference in work functions [57]. This caused the transfer of electrons from a material with a lower work function to another material with a higher work function to equilibrate and generate a new Fermi level [58]. Since the work functions of AgBr and AgCl are greater than that of Ag (Φ_{AgBr} = 5.3 eV, Φ_{AgCl} = 4.8 eV and Φ_{Ag} = 4.25 eV) [58,59], and the Fermi levels of AgBr and AgCl are lower than that of Ag, the transfer of photogenerated electrons can easily occur from the plasmonic Ag to the CB of AgX [18,20,60–62].
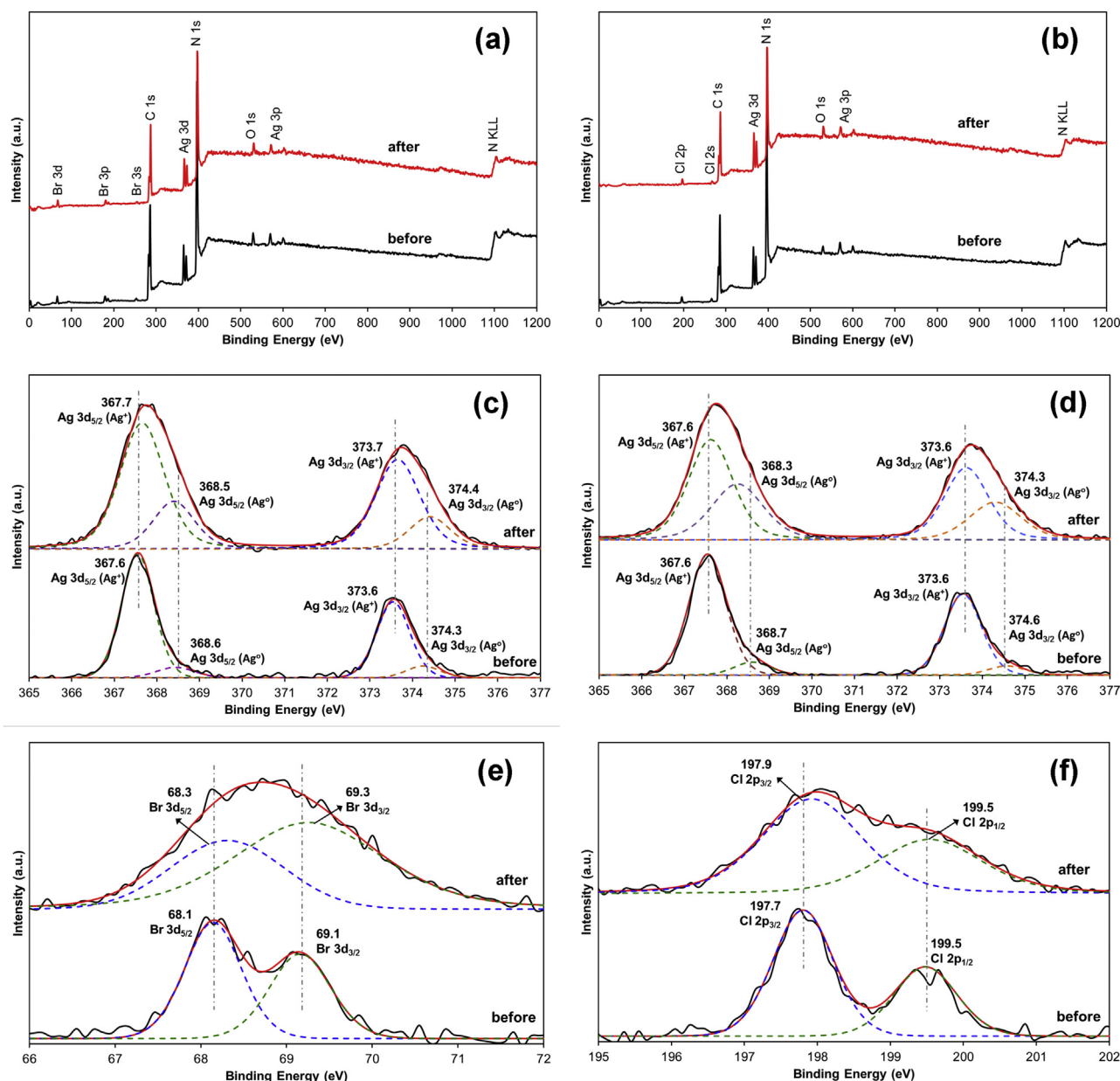
Fig. 11. XPS survey spectra of the (a) 30AgBr/pCN and (b) 30AgCl/pCN samples before and after the photocatalytic reactions for four times. High resolution XPS spectra of (c) Ag 3d and (e) Br 3d of 30AgBr/pCN sample before and after the photocatalytic reactions. High resolution XPS spectra of (d) Ag 3d and (f) Cl 2p of 30AgCl/pCN sample before and after the photocatalytic reactions.

Meanwhile, in the hybridization of AgX nanoparticles with pCN, the heterojunction interface was developed when these two semiconductor photocatalysts with different VB and CB potentials were coupled together. It is anticipated that the enhancement in the photoactivity is principally influenced by the efficient charge transfer across the heterojunction and also the band alignments with respect to the desired reduction potential [63]. Possible photocatalytic reaction mechanisms on the AgBr/pCN and AgCl/pCN hybrid nanocomposites were discussed below. From Fig. 12, photoinduced charge carriers were transferred across the heterojunction in both AgBr/pCN and AgCl/pCN systems. The band edge (VB and CB) positions of each semiconductor were calculated using the Mulliken electronegativity theory as exemplified below [9,42,64].

$$E_{CB} = X - E_C - \frac{1}{2}E_g \qquad (2)$$

where E_{CB} and E_{VB} are the CB minimum and VB maximum relative to the normal hydrogen electrode (NHE), E_c is the energy of free electrons on hydrogen scale taken as 4.5 eV, E_g is the band gap energy of the semiconductor and X is the geometric mean of the absolute electronegativity of the constituent atoms, which is the arithmetic mean of the atomic electron affinity and ionization energy. Based on Eq. (2), the positions of VB and CB edge of AgBr and AgCl were at +1.70 and −0.90 eV, and +2.00 and −1.20 eV, respectively. Meanwhile, for pCN, the VB and CB potentials were determined to be +1.65 and −1.15 eV, respectively.

In this case, the CB potential of pCN was more negative than that of AgBr, but less negative than that of AgCl. On the other hand, the VB potential of pCN was less positive than that of AgBr and AgCl. As a result, the resulting hybrid heterojunction could be classified into two different types (denoted as Type I and Type II) when pCN was in direct contact with (1) AgCl and (2) AgBr, as schematically
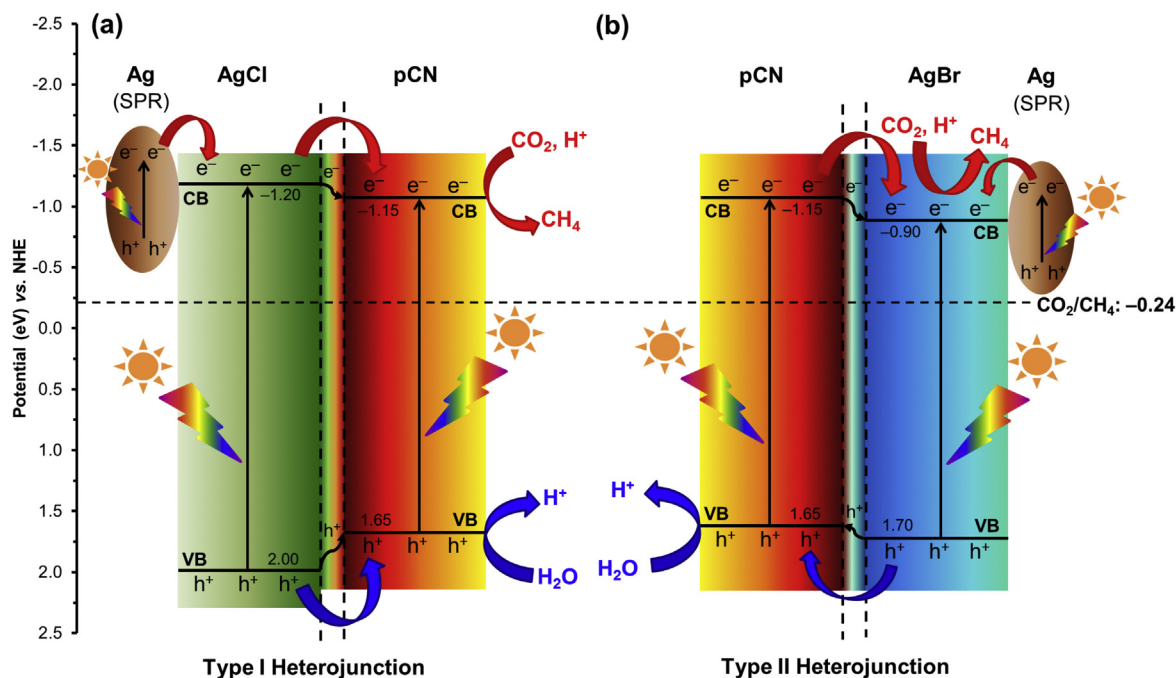
Fig. 12. Schematic illustration of the band structures of (a) Ag/AgCl/pCN and (b) Ag/AgBr/pCN hybrid nanocomposites for the photoreduction of CO_2 with H_2O to CH_4 under the light irradiation.
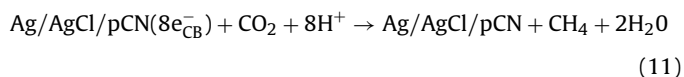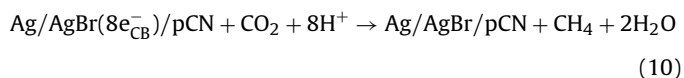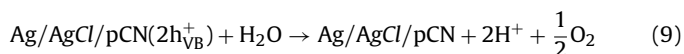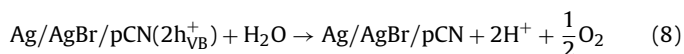
presented in Fig. 12. Upon light irradiation, both pCN and AgX in the hybrid heterostructures generated electron–hole pairs and then the charge transfer across the heterojunction would follow either Type I or Type II. For the Type I heterojunction (Fig. 12a), which was demonstrated by the Ag/AgCl/pCN sample, the VB and CB potentials of AgCl enveloped both the VB and CB potentials of pCN. Due to the SPR effect from metallic Ag and the fact that the CB edge of AgCl (−1.20 eV) was more negative than that of pCN (−1.15 eV), the excited electrons were transferred from Ag and AgCl to the CB of pCN. Additionally, the photogenerated holes were transported from AgCl to pCN to oxidize H_2O to protons (H^+). On account of the relative negative CB potential of pCN (−1.15 eV vs. NHE) to CO_2/CH_4 (−0.24 V vs. NHE), the stored electrons on the CB of pCN could readily convert CO_2 to CH_4 in the presence of H^+. However, the drawback of Type I heterojunction system was that the charge carriers from pCN and AgCl were accumulated in the pCN, resulting in a higher recombination rate and impairing the photocatalytic activity. Thus, no overall improvement in the separation efficiency of charge carriers could be achieved in the Ag/AgCl/pCN hybrid nanostructures (upon photoreduction).

In contrary, for the Type II heterojunction (Fig. 12b), which was exhibited by the Ag/AgBr/pCN sample, the photogenerated electrons and holes were spatially separated by migrating the charge carriers apart from each semiconductor. In other words, the SPR-excited electrons from Ag and the photogenerated electrons from the CB of pCN were injected to the CB of AgBr, whereas the holes were transported from the VB of AgBr to that of pCN. This promoted the efficient separation of electron-hole pairs due to the well-matched energy bands of pCN, Ag and AgBr. Hence, the well-contacted interface between pCN and plasmonic Ag/AgBr (upon photoreduction) in the heterostructured nanocomposites would hinder the recombination process of charge carriers, leading to an improved photoactivity. Evidently, based on the thermodynamic viewpoint, the CB of AgBr was more negative (−0.90 eV vs. NHE) than that of the potential CO_2/CH_4 (−0.24 V vs. NHE). This rendered the enriched electrons on the CB of AgBr to reduce CO_2 in the presence of H^+ to CH_4. The H^+ was originated from the H_2O oxidation by the accumulated holes on the pCN.

Furthermore, in terms of reaction kinetic, which is expressed by the thermodynamic driving force (ΔE) between the reduction potential of CO_2/CH_4 and the CB potential of the semiconductor upon electron transfer, it was found that the ΔE of the Ag/AgCl/pCN was greater (0.91 eV) than that of Ag/AgBr/pCN (0.66 eV). It is known that a larger ΔE favors a higher reaction rate [40]. However, in this situation, the photocatalytic results of 30Ag/AgBr/pCN and 30Ag/AgCl/pCN did not display such a trend due to the fact that Ag/AgCl/pCN possessed the Type I heterojunction structure, which would in turn increase the recombination rate of electron–hole pairs, resulting in a lower CH_4 evolution. As seen in Fig. 12a, the photogenerated charge carriers were accumulated in the pCN instead. As a result, the benefit of a larger ΔE in Ag/AgCl/pCN was compensated. This phenomenon was concordant with the PL results (Fig. 9B), in which the PL intensity of 30AgBr/pCN was lower than that of 30AgCl/pCN.

The main reaction steps involved in the CO_2 photoreduction were summarized by Eqs. (3)–(11). Overall, it can be concluded that the high photocatalytic activity of Ag/AgBr/pCN over the Ag/AgCl/pCN hybrid nanoarchitectures was attained owing to the synergistic interactions of the SPR effect from Ag due to photoreduction of some AgBr nanoparticles as well as well-aligned band potentials in the hybrid nanocomposites for effective interfacial charge transfer across the heterojunction. Therefore, the manipulation of semiconductor heterojunctions by incorporating pCN with AgX of appropriate VB and CB edges is of crucial importance for improved catalytic activity.

$$AgBr \xrightarrow{h\nu} AgBr(e_{CB}^-) + AgBr(h_{VB}^+) \tag{3}$$

$$AgCl \xrightarrow{h\nu} AgCl(e_{CB}^-) + AgCl(h_{VB}^+) \tag{4}$$

$$Ag^+ + e_{CB}^- \rightarrow Ag^0 \tag{5}$$

$$Ag^0 \xrightarrow{h\nu(SPR)} Ag^+ + e^- \tag{6}$$

$$pCN \xrightarrow{h\nu} pCN(e_{CB}^-) + pCN(h_{VB}^+) \tag{7}$$

$$Ag/AgBr/pCN(2h^+_{VB}) + H_2O \rightarrow Ag/AgBr/pCN + 2H^+ + \frac{1}{2}O_2 \qquad (8)$$

$$Ag/AgCl/pCN(2h^+_{VB}) + H_2O \rightarrow Ag/AgCl/pCN + 2H^+ + \frac{1}{2}O_2 \qquad (9)$$

$$Ag/AgBr(8e^-_{CB})/pCN + CO_2 + 8H^+ \rightarrow Ag/AgBr/pCN + CH_4 + 2H_2O \qquad (10)$$

$$Ag/AgCl/pCN(8e^-_{CB}) + CO_2 + 8H^+ \rightarrow Ag/AgCl/pCN + CH_4 + 2H_2O \qquad (11)$$

4. Conclusions

In summary, AgX/pCN(X = Cl and Br) heterojunction photocatalysts were successfully synthesized at room temperature via a sonication-assisted deposition-precipitation strategy. The as-prepared AgX/pCN photocatalysts showed enhanced reduction of CO_2 to CH_4 under a low-power energy-saving daylight bulb at ambient temperature and atmospheric pressure. The results demonstrated that the optimal 30AgBr/pCN sample showed the highest photocatalytic performance, which manifested a noteworthy 34.1- and 4.2-fold enhancement in the CH_4 evolution over pure AgBr and pCN, respectively. Additionally, by comparing different halide ions, the photocatalytic activity of 30AgBr/pCN was higher (by a factor of 1.3) than that of the optimal 30AgCl/pCN. Such a remarkable improvement in the photocatalytic performance of 30AgBr/pCN was mainly ascribed to the enhanced separation efficiency of photogenerated electron–hole pairs at the heterojunction interface of AgBr/pCN hybrid nanostructures. This was attributed to the well-matched overlapping band potentials of pCN and AgBr, which possessed Type II heterojunction (as supported by PL studies). Additionally, the formation of metallic Ag upon reduction of some AgBr nanoparticles during the photocatalytic process (as evidenced by XPS analysis) played a prominent role in the localized SPR effect by absorbing the visible light, thus generating electron-hole pairs. This further promoted the interfacial charge transfer across the Ag/AgBr interface by providing more free electrons for the CO_2 reduction to take place. More importantly, the as-developed 30AgBr/pCN photocatalyst exemplified a high photostability and recyclability after four successive cycles without an obvious decrease in the total CH_4 production. As a whole, the present work provides a new doorway on the development of plasmon-based g-C_3N_4 heterojunction nanocomposites with efficient charge transfer and separation toward diverse photoredox applications for environmental remediation and solar energy conversion.

Acknowledgements

Appendix A. Supplementary data

Supplementary data associated with this article can be found, in the online version, at http://dx.doi.org/10.1016/j.apcatb.2015.06.053

References

[1] I. Shown, H.-C. Hsu, Y.-C. Chang, C.-H. Lin, P.K. Roy, A. Ganguly, C.-H. Wang, J.-K. Chang, C.-I. Wu, L.-C. Chen, K.-H. Chen, Nano Lett. 14 (2014) 6097–6103.
[2] W.-J. Ong, L.-L. Tan, S.-P. Chai, S.-T. Yong, A.R. Mohamed, ChemSusChem 7 (2014) 690–719.
[3] Z.Q. He, D. Wang, H.Y. Fang, J.M. Chen, S. Song, Nanoscale 6 (2014) 10540–10544.
[4] S. Xie, Y. Wang, Q. Zhang, W. Deng, Y. Wang, ACS Catal. 4 (2014) 3644–3653.
[5] W.-J. Ong, L.-L. Tan, S.-P. Chai, S.-T. Yong, A.R. Mohamed, Nano Res. 7 (2014) 1528–1547.
[6] W.-J. Ong, L.-L. Tan, S.-P. Chai, S.-T. Yong, A.R. Mohamed, Nanoscale 6 (2014) 1946–2008.
[7] G. Xi, S. Ouyang, P. Li, J. Ye, Q. Ma, N. Su, H. Bai, C. Wang, Angew. Chem. Int. Ed. 51 (2012) 2395–2399.
[8] K. Iizuka, T. Wato, Y. Miseki, K. Saito, A. Kudo, J. Am. Chem. Soc. 133 (2011) 20863–20868.
[9] H. Shi, G. Chen, C. Zhang, Z. Zou, ACS Catal. 4 (2014) 3637–3643.
[10] X. Wang, K. Maeda, A. Thomas, K. Takanabe, G. Xin, J.M. Carlsson, K. Domen, M. Antonietti, Nat. Mater. 8 (2009) 76–80.
[11] Y. Wang, R. Shi, J. Lin, Y. Zhu, Energy Environ. Sci. 4 (2011) 2922–2929.
[12] M.J. Munoz-Batista, A. Kubacka, M. Fernandez-Garcia, Catal. Sci. Technol. 4 (2014) 2006–2015.
[13] Y. Tian, B. Chang, J. Lu, J. Fu, F. Xi, X. Dong, ACS Appl. Mater. Interfaces 5 (2013) 7079–7085.
[14] Z. Jin, N. Murakami, T. Tsubota, T. Ohno, Appl. Catal. B 150–151 (2014) 479–485.
[15] W.-J. Ong, L.-L. Tan, S.-P. Chai, S.-T. Yong, Chem. Commun. 51 (2015) 858–861.
[16] W.-J. Ong, L.-L. Tan, S.-P. Chai, S.-T. Yong, Dalton Trans. 44 (2015) 1249–1257.
[17] H. Xu, J. Yan, Y. Xu, Y. Song, H. Li, J. Xia, C. Huang, H. Wan, Appl. Catal. B 129 (2013) 182–193.
[18] H. Shi, J. Chen, G. Li, X. Nie, H. Zhao, P.-K. Wong, T. An, ACS Appl. Mater. Interfaces 5 (2013) 6959–6967.
[19] S. Zhang, J. Li, X. Wang, Y. Huang, M. Zeng, J. Xu, ACS Appl. Mater. Interfaces 6 (2014) 22116–22125.
[20] Y.-S. Xu, W.-D. Zhang, ChemCatChem 5 (2013) 2343–2351.
[21] Y. Yang, W. Guo, Y. Guo, Y. Zhao, X. Yuan, Y. Guo, J. Hazard. Mater. 271 (2014) 150–159.
[22] W.-J. Ong, L.-L. Tan, S.-P. Chai, S.-T. Yong, A.R. Mohamed, Nano Energy 13 (2015) 757–770.
[23] L.-L. Tan, W.-J. Ong, S.-P. Chai, A.R. Mohamed, Appl. Catal. B 166–167 (2015) 251–259.
[24] L.-L. Tan, W.-J. Ong, S.-P. Chai, A.R. Mohamed, Chem. Commun. 50 (2014) 6923–6926.
[25] J. Oh, S. Lee, K. Zhang, J.O. Hwang, J. Han, G. Park, S.O. Kim, J.H. Park, S. Park, Carbon 66 (2014) 119–125.
[26] Z. Chen, P. Sun, B. Fan, Z. Zhang, X. Fang, J. Phys. Chem. C 118 (2014) 7801–7807.
[27] Y. Lan, X. Qian, C. Zhao, Z. Zhang, X. Chen, Z. Li, J. Colloid Interface Sci. 395 (2013) 75–80.
[28] Y. He, Y. Wang, L. Zhang, B. Teng, M. Fan, Appl. Catal. B 168–169 (2015) 1–8.
[29] B. Cai, J. Wang, S. Gan, D. Han, Z. Wu, L. Niu, J. Mater. Chem. A 2 (2014) 5280–5286.
[30] C. Han, Y. Wang, Y. Lei, B. Wang, N. Wu, Q. Shi, Q. Li, Nano Res. 8 (2015) 1199–1209.
[31] Z. Zhang, J. Huang, M. Zhang, Q. Yuan, B. Dong, Appl. Catal. B 163 (2015) 298–305.
[32] P. Niu, Y. Yang, J.C. Yu, G. Liu, H.-M. Cheng, Chem. Commun. 50 (2014) 10837–10840.
[33] X. Lu, K. Xu, P. Chen, K. Jia, S. Liu, C. Wu, J. Mater. Chem. A 2 (2014) 18924–18928.
[34] W. Ma, D. Han, M. Zhou, H. Sun, L. Wang, X. Dong, L. Niu, Chem. Sci. 5 (2014) 3946–3951.
[35] Y. Zheng, L. Lin, X. Ye, F. Guo, X. Wang, Angew. Chem. Int. Ed. 53 (2014) 11926–11930.
[36] G. Zhang, C. Huang, X. Wang, Small 11 (2015) 1215–1221.
[37] J. Duan, S. Chen, M. Jaroniec, S.Z. Qiao, ACS Nano 9 (2015) 931–940.
[38] Y. Hou, Z. Wen, S. Cui, X. Guo, J. Chen, Adv. Mater. 25 (2013) 6291–6297.
[39] T.Y. Ma, Y. Tang, S. Dai, S.Z. Qiao, Small 10 (2014) 2382–2389.
[40] Z.a. Huang, Q. Sun, K. Lv, Z. Zhang, M. Li, B. Li, Appl. Catal. B 164 (2015) 420–427.
[41] M. Lu, Z. Pei, S. Weng, W. Feng, Z. Fang, Z. Zheng, M. Huang, P. Liu, Phys. Chem. Chem. Phys. 16 (2014) 21280–21288.
[42] C. An, J. Wang, W. Jiang, M. Zhang, X. Ming, S. Wang, Q. Zhang, Nanoscale 4 (2012) 5646–5650.
[43] M. Zhang, X. Wang, Energy Environ. Sci. 7 (2014) 1902–1906.
[44] D.J. Martin, K. Qiu, S.A. Shevlin, A.D. Handoko, X. Chen, Z. Guo, J. Tang, Angew. Chem. Int. Ed. 53 (2014) 9240–9245.
[45] W.-J. Ong, J.-J. Yeong, L.-L. Tan, B.T. Goh, S.-T. Yong, S.-P. Chai, RSC Adv. 4 (2014) 59676–59685.
[46] Q. Xiang, J. Yu, M. Jaroniec, J. Am. Chem. Soc. 134 (2012) 6575–6578.
[47] S. Feng, X. Chen, Y. Zhou, W. Tu, P. Li, H. Li, Z. Zou, Nanoscale 6 (2014) 1896–1900.
[48] Y. Liu, S. Zhou, J. Li, Y. Wang, G. Jiang, Z. Zhao, B. Liu, X. Gong, A. Duan, J. Liu, Y. Wei, L. Zhang, Appl. Catal. B 168–169 (2015) 125–131.
[49] M. Li, L. Zhang, X. Fan, Y. Zhou, M. Wu, J. Shi, J. Mater. Chem. A 3 (2015) 5189–5196.
[50] L. Liu, H. Zhao, J.M. Andino, Y. Li, ACS Catal. 2 (2012) 1817–1828.
[51] J. Yu, J. Jin, B. Cheng, M. Jaroniec, J. Mater. Chem. A 2 (2014) 3407–3416.

[52] W.-N. Wang, W.-J. An, B. Ramalingam, S. Mukherjee, D.M. Niedzwiedzki, S. Gangopadhyay, P. Biswas, J. Am. Chem. Soc. 134 (2012) 11276–11281.
[53] W.-J. Ong, M.M. Gui, S.-P. Chai, A.R. Mohamed, RSC Adv. 3 (2013) 4505–4509.
[54] X. Yao, X. Liu, X. Hu, ChemCatChem 6 (2014) 3409–3418.
[55] C. Han, L. Ge, C. Chen, Y. Li, Z. Zhao, X. Xiao, Z. Li, J. Zhang, J. Mater. Chem. A 2 (2014) 12594–12600.
[56] B. Tian, R. Dong, J. Zhang, S. Bao, F. Yang, J. Zhang, Appl. Catal. B 158–159 (2014) 76–84.
[57] W.-S. Wang, H. Du, R.-X. Wang, T. Wen, A.-W. Xu, Nanoscale 5 (2013) 3315–3321.
[58] G. Wang, H. Mitomo, Y. Matsuo, N. Shimamoto, K. Niikura, K. Ijiro, J. Mater. Chem. B 1 (2013) 5899–5907.

[59] J. Jiang, H. Li, L. Zhang, Chem. Eur. J. 18 (2012) 6360–6369.
[60] D. Chen, Z. Wang, Y. Du, G. Yang, T. Ren, H. Ding, Catal. Today (2015), http://dx.doi.org/10.1016/j.cattod.2015.1003.1031
[61] S. Linic, P. Christopher, D.B. Ingram, Nat. Mater. 10 (2011) 911–921.
[62] X. Li, S. Fang, L. Ge, C. Han, P. Qiu, W. Liu, Appl. Catal. B 176–177 (2015) 62–69.
[63] S. Zhou, Y. Liu, J. Li, Y. Wang, G. Jiang, Z. Zhao, D. Wang, A. Duan, J. Liu, Y. Wei, Appl. Catal. B 158–159 (2014) 20–29.
[64] W.-J. Ong, S.-Y. Voon, L.-L. Tan, B.T. Goh, S.-T. Yong, S.-P. Chai, Ind. Eng. Chem. Res. 53 (2014) 17333–17344.